

pubs.acs.org/cm Article

# Ordering and Structural Transformations in Layered K<sub>x</sub>CrO<sub>2</sub> for K-Ion Batteries

Jonas L. Kaufman and Anton Van der Ven\*



Cite This: Chem. Mater. 2020, 32, 6392-6400



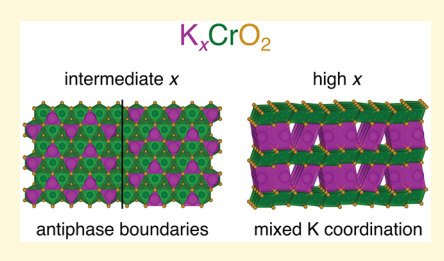
**ACCESS** I

Metrics & More



Supporting Information

**ABSTRACT:** The success of K-ion battery technology will rely on the development of robust cathode materials that can incorporate and shuttle large amounts of K reversibly. Recent experimental work has demonstrated the viability of layered KCrO<sub>2</sub> as a cathode material for K-ion batteries; however, some fundamental details of structural phase transitions and K ordering during cycling remain unknown. We report on a first-principles thermodynamic investigation of layered  $K_x \text{CrO}_2$  ( $0 \le x \le 1$ ) in the O3 and P3 host structures. We predict that P3 is preferred at intermediate x, with the stable K orderings belonging to staircases of phases that contain antiphase boundaries between ordered regions. Varying densities of these boundaries allow for smooth changes in composition.



At high x, we predict the stability of "M" phases containing a mixture of octahedral and prismatic K coordination within each layer, which is accommodated by undulations of the oxide host. Our calculated voltage curve and analysis of structural evolution indicate that the predicted phase stability, including the formation of the M phases, is mostly compatible with experimental observations.

# 1. INTRODUCTION

There is a consensus that deep decarbonization efforts must include extensive electrification across industries, which in turn will require reliable and cost-effective options for grid energy storage. Rechargeable Li-ion batteries are well suited for short-duration storage needs, but alternative technologies are highly desirable to avoid supply problems related to Li and other constituents. Na- and K-ion batteries have emerged as potential replacements for Li-ion batteries in such applications, mostly due to the far greater abundance of those elements. Compared to Na, K offers several additional advantages: Its lower redox potential can yield higher voltages and it can reversibly intercalate into graphite anodes. Signature in the such as th

Several classes of materials have been investigated as cathodes for K-ion batteries, including the familiar layered transition-metal oxides used in Li- and Na-ion batteries. 5,7,8 The layered oxides generally promise high theoretical energy density and rate capability.<sup>8,9</sup> However, almost all of the layered oxide K intercalation compounds investigated thus far, such as K<sub>x</sub>MnO<sub>2</sub> and K<sub>x</sub>CoO<sub>2</sub>, have only been synthesized and cycled at intermediate K concentration x, limiting their practical capacities. An important exception is layered KCrO<sub>2</sub>, first synthesized by Delmas et al., <sup>21,22</sup> which is stable in the fully potassiated limit. In a key breakthrough, Kim et al. recently showed that this stability is unique to Cr (among redox-active 3d transition metals) and demonstrated the cyclability of layered KCrO2 in electrochemical cells over a wide range of K concentrations. 23 Other studies have examined K-deficient K<sub>x</sub>CrO<sub>2</sub> starting materials, <sup>24,25</sup> which display different cycling behaviors. This variation in experimental observations necessitates an understanding of the equilibrium thermodynamics of this system.

While KCrO<sub>2</sub> is a viable candidate cathode material for K-ion batteries, questions remain about its structural evolution during cycling, which directly impacts battery performance. As observed by Kim et al., the system displays a multitude of different phases upon deintercalation, which produces a complex, stepwise voltage profile not unlike those of many layered Na intercalation compounds.<sup>23</sup> Phase transitions occur between the layered O3 and P3 structures (O/P denote octahedral/prismatic K coordination), shown in Figure 1, as

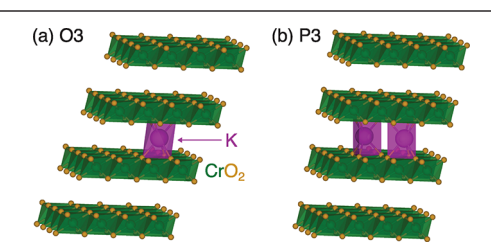


**Figure 1.** (a) O3 and (b) P3 host structures of  $K_x CrO_2$ , which alternate between slabs of edge-sharing  $CrO_6$  octahedra and K intercalation layers. The O3 structure allows K to lie on octahedral sites on a single triangular lattice, while the P3 structure allows K to lie on prismatic sites on either of two triangular lattices. Structures visualized using VESTA.<sup>29</sup>

Received: April 5, 2020 Revised: July 7, 2020 Published: July 8, 2020





well as O'3 and P'3 (primes indicate monoclinic distortions of the hexagonal parent structures<sup>26</sup>). Such transitions are accommodated by the facile sliding of  $CrO_2$  layers.<sup>27,28</sup> The details of structural phase stability and K ordering preferences are currently unknown for  $K_xCrO_2$ . Kim et al.<sup>23</sup> found that a significant fraction of the capacity is lost after the first charge, which may be related to the irreversibility of certain transitions. Elucidating the nature of structural changes and K-ordering transitions will assist the engineering of Cr-based cathodes for next-generation K-ion batteries.

Here we describe the results of a comprehensive firstprinciples study of the phase stability of K<sub>r</sub>CrO<sub>2</sub> as a function of x ( $0 \le x \le 1$ ). We predict a myriad of ground state and low energy orderings in P3 at intermediate K concentrations that belong to several families of hierarchical phases. These phases consist of periodic arrays of antiphase boundaries that separate well-ordered domains. We also predict the stability of a family of undulating phases with a mixture of octahedral and prismatic coordination within the same K intercalation layer at high K concentrations. The undulating phases are referred to as M phases as they host mixed K coordination. An analysis of simulated diffraction patterns of the M phases suggests that they may have already been observed experimentally, being mistaken for O'3. We argue that the large elastic deformations that are required to form the M phases may explain experimentally observed capacity losses at high K concentrations.

#### 2. METHODS

Total energies were calculated from density functional theory (DFT) using the Vienna *ab initio* Simulation Package (VASP).  $^{30-33}$  The K sv, Cr pv, and O projector augmented wave (PAW) pseudopotentials  $^{34,35}$  were used with a plane-wave energy cutoff of 600 eV, which, during testing, was found to be sufficient for convergence of energy differences to within 0.6 meV/CrO<sub>2</sub>. Γ-centered Monkhorst–Pack *k*-meshes were automatically generated with a density of 34 Å, which, during testing, was found to be sufficient for convergence of total energies to within 0.1 meV/CrO<sub>2</sub>. The SCAN meta-GGA functional was employed to approximate the exchange-correlation energy, as it has been found to produce an improved description of layered oxides compared to GGA(+U).  $^{23,39-41}$  Spin-polarization was enabled, and all moments were initialized ferromagnetically unless otherwise noted. Structures were relaxed until the forces were smaller than 0.02 eV/Å, prior to performing final static calculations using the linear tetrahedron method.  $^{42}$ 

Symmetrically distinct K/vacancy-ordered configurations within periodic supercells of the O3 and P3 host structures were enumerated using the Clusters Approach to Statistical Mechanics (CASM) software package. 43-46 Energies were calculated for 219 O3 configurations, 258 P3 configurations, and 39 M configurations. The M structures relaxed from certain O3 configurations and were identified visually and by the deformation scores calculated by CASM. The majority of P3 configurations considered in this study were limited to those that do not contain a nearest-neighbor (NN) K-K pair, as configurations with such pairs were found to be highly unstable due to steric repulsion. Some nonferromagnetic orderings of Cr spins were considered for the O3-KCrO<sub>2</sub> and P3-K<sub>1/2</sub>CrO<sub>2</sub> ground state structures. Cluster expansion effective Hamiltonians for the O3 and P3 structures were fit iteratively in order to predict low-energy configurations and to run grand canonical Monte Carlo simulations of finite-temperature phase stability. For P3, the effective cluster interaction of the NN pair was manually set to a large value (5 eV/ pair) to ensure no simultaneous occupation of those sites in our cluster expansion predictions. Details of the cluster expansions and Monte Carlo simulations can be found in Sections S1 and S2 of the Supporting Information, respectively.

Voltage was calculated using the Nernst equation<sup>47</sup>

$$V = -\frac{\mu_{\rm K} - \mu_{\rm K}^{\circ}}{e} \tag{1}$$

where  $\mu_K$  is the K chemical potential of  $K_x Cr O_2$ ,  $\mu_K^o$  is the reference chemical potential of K metal in the body-centered cubic structure, and e is the elementary charge.

#### 3. RESULTS

**3.1. Phase Stability and Voltage.** Figure 2a shows the calculated zero-temperature formation energies of configu-

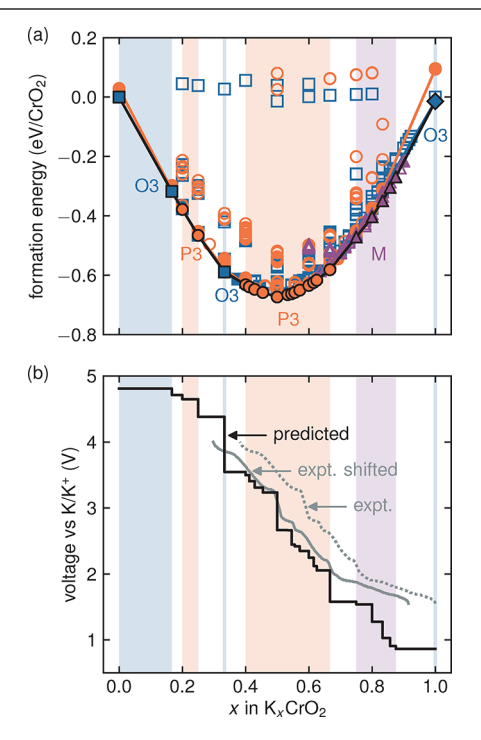


Figure 2. (a) Formation energy vs composition for calculated configurations. Filled symbols denote configurations on the local hull of each host structure. The global hull is outlined in black. Colored regions in the background indicate where each host structure is globally stable. The diamond at x=1 indicates an antiferromagnetic ordering in O3. All other configurations shown are ferromagnetic. (b) Voltage vs composition as predicted by DFT (black) compared to an experimentally measured first charge curve from Kim et al. (gray, taken from Figure 3a of ref 23). The original experimental curve is shown as a dotted line, while the solid line is shifted in composition by  $\Delta x = -0.085$ .

rations within each host structure (O3, P3, or M). Formation energies were calculated relative to CrO<sub>2</sub> and KCrO<sub>2</sub> in the O3 structure. The convex hulls are shown for each host individually, along with the global convex hull of ground states over all host structures. O3 is predicted to be stable for 0  $\leq x \leq 1/6$ , x = 1/3, and x = 1, P3 is predicted to be stable for  $1/5 \le x \le 1/4$  and  $2/5 \le x \le 2/3$ , and M is predicted to be stable for  $3/4 \le x \le 7/8$ . The set of high-energy (near zero formation energy) configurations in O3 and P3 at intermediate concentrations correspond to staged structures in which all layers are either completely empty or completely filled. Figure S2 of the Supporting Information plots the distance of each formation energy to the global hull in order to more clearly reveal structures that are close to the global hull. A high degree of degeneracy is predicted among different host structures and ordered K-vacancy configurations. For example, the energy

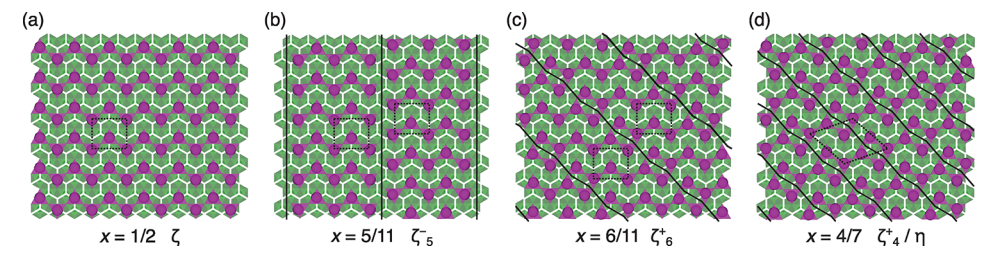


Figure 3. Relaxed in-plane K orderings of the (a) x = 1/2, (b) x = 5/11, (c) x = 6/11, and (d) x = 4/7 ground states in P3. The honeycomb network of available prismatic sites is shown in white. Black solid lines indicate antiphase boundaries. Black dotted lines indicated the in-layer unit cells of the ζ ordering (a-c) and the η ordering (d). Structures visualized using VESTA.

difference between the O3 and the P3 ground states at x=1/5 and x=1/4 is less than 2.5 meV/CrO<sub>2</sub>, indicating that the two host structures are nearly degenerate at these compositions considering the accuracy of the DFT calculations. We did not exhaustively explore the phase stability below x=1/3, given that this region is above the voltage interval that has been reversibly accessed experimentally. Fully deintercalated layered oxides often prefer the O1 structure; however, we calculated the energy of O1-CrO<sub>2</sub> to be 1.0 meV/CrO<sub>2</sub> higher than that of O3-CrO<sub>2</sub>. We therefore did not consider any staged hybrid structures with alternating O1- and O3-type stacking at low x.

All formation energies plotted in Figure 2a, with the exception of O3 KCrO2, were calculated with a ferromagnetic (FM) configuration. The O3 ground state at x = 1 (indicated by a diamond in Figure 2a) has an antiferromagnetic (AFM) in-layer ordering of the Cr spins (Figure S3a, Supporting Information). This ordering is 14 meV/CrO<sub>2</sub> lower in energy than the FM configuration of KCrO<sub>2</sub>. A preference for AFM ordering is consistent with the low-temperature magnetic behavior observed experimentally in KCrO<sub>2</sub>. 50,51 The P3 ground state at x = 1/2, in contrast, prefers a FM in-layer ordering, with negligible magnetic interactions between adjacent CrO<sub>2</sub> layers (Figure S3b, Supporting Information). The FM x = 1/2 ground state was predicted to be 17 meV/ CrO<sub>2</sub> more stable than the closest non-FM in-layer ordering considered in this study. We therefore performed all other calculations ferromagnetically.

Figure 2b shows the zero-temperature equilibrium voltage curve obtained by calculating the K chemical potential using the global hull formation energies of Figure 2a. The numerous ground state orderings in P3 produce a series of small steps in the voltage curve, along with larger steps at x = 1/2, 6/11, and 2/3. The M ground states yield another staircase of steps at higher composition, while the O3 ground state at x = 1/3produces a large step. Generally, plateaus in the equilibrium voltage profile signify the occurrence of first-order phase transitions, as they correspond to a discontinuous jump in composition at a constant K chemical potential. In the case of the ordered phases that we describe in Section 3.2, computational constraints limit us to examining a finite number of orderings, which results in a stepped voltage profile. However, an actual material will have the flexibility to sample a much larger number of phases that are separated by much smaller composition intervals, thereby giving the impression of a smoother, sloping voltage profile.

A first-charge voltage curve measured by Kim et al.<sup>23</sup> is also plotted in Figure 2b. The reported capacity for the experimental voltage curve was converted to composition based on the theoretical capacity of KCrO<sub>2</sub>. Figure 2b also

shows the same experimental voltage curve shifted by  $\Delta x =$ -0.085, such that the largest step coincides with the x = 1/2ordering in P3. Such a shift is appropriate, as Kim et al.<sup>23</sup> observed that some K is extracted from the stoichiometric KCrO<sub>2</sub> starting material before cycling. They attributed this to interaction with the carbon that was added to the electrode. A rigid shift in composition is the only adjustment we can include in our comparison without making assumptions about other factors such as side reactions. We also note that the chemical potential gradients present in real systems typically introduce polarization, whereby the measured voltage lies above and below the equilibrium voltage on charge and discharge, respectively,<sup>52</sup> though we have not considered this in our comparison. After accounting for the shift in composition, the quantitative and qualitative agreement between our predicted voltage curve and experiment is quite good. In particular, the three major steps in the experimental curve match those predicted at x = 1/2, 6/11, and 2/3, with sloping regions in between that are consistent with many smaller steps.

Our grand canonical Monte Carlo simulations (described in Section S2, Supporting Information) suggest that the O3 and P3 ground states for  $x \ge 1/3$  do not disorder at 300 K (Figure S1, Supporting Information). The cluster expansion and Monte Carlo approach can overestimate order-disorder transition temperatures; however, we also saw no significant disordering of the ground states up to around 500 K (Figure S1, Supporting Information). This is consistent with the strong ordering preferences displayed by related systems such as Na<sub>x</sub>CoO<sub>2</sub>. 53 The highly distorted nature of the M phases (see Section 3.2) makes them difficult to model with a configurational cluster expansion approach, but the coupling of K ordering to periodic undulations of the host layers likely limits the ability of the M phases to accommodate disorder. It is, therefore, reasonable to treat each M phase as a line compound with its free energy approximated by its DFT formation energy.

**3.2. Ground State Orderings.** As shown in Figure 2, many ordered phases appear over a wide range of compositions in  $K_xCrO_2$ . We focus on the P3 and M ground states, as these appear in the experimentally accessed composition interval. The ground state orderings found in P3 (for  $2/5 \le x \le 2/3$ ) belong to several families of hierarchical orderings first identified in  $Na_xCoO_2$  and later predicted for  $K_xCoO_2$ . These phases consist of regions of a single in-layer ordering separated by antiphase boundaries (APBs) that accommodate additional K or vacancies, thereby allowing for smooth variations in composition. This is illustrated in Figure 3. The x = 1/2 ordering (Figure 3a), which has been labeled  $\zeta_r^{53}$  corresponds to the familiar zigzag row ordering on the honeycomb network that has been observed in several Na

systems with the P3 structure. S5,56 Below x=1/2, the  $\zeta$  ordering is maintained locally while vacancies accumulate along periodically spaced APBs as shown in Figure 3b. Above x=1/2, the excess K concentrates along the APBs shown in Figure 3c. We have labeled the families of orderings immediately below and above x=1/2 as the  $\zeta^-$  and  $\zeta^+$  phases, respectively. At x=4/7 we predict an important  $\zeta^+$  ground state having the maximum possible density of APBs (Figure 3d). This ordering has been labeled  $\eta$  to distinguish it from the other  $\zeta^+$  phases. It forms the basis of a third family of orderings ( $\eta^+$ ) for  $4/7 < x \le 2/3$  that consist of  $\eta$  domains separated by APBs that introduce additional K. A complete description of the  $\zeta^-$ ,  $\zeta^+$ , and  $\eta^+$  orderings can be found in ref 53.

The hierarchy of ground state orderings in P3 has the flexibility to vary the K concentration almost continuously without significantly disrupting strong local ordering preferences. This is achieved by varying the density of APBs. Orderings within the hierarchy can, therefore, be enumerated algorithmically by varying the periodicity with which APBs occur. This was done to systematically enumerate 3387 hierarchical orderings in an automated fashion. We generated all in-layer  $\zeta^-$ ,  $\zeta^+$ , and  $\eta^+$  orderings in supercells of volume 36 times the primitive cell volume or less, as well as all symmetrically distinct stackings of those orderings. We subsequently approximated their energies using the cluster expansion developed for the P3 host. There is typically a large number of these orderings at a given composition because different spacings of APBs can yield the same composition, 53 as do different stackings of the same in-layer ordering. To summarize, all 3387 configurations enumerated belong to one of the three families of APB-based orderings, allowing us to assess the energetics of these orderings across many more compositions than we investigated with DFT. As shown in Figure 4, the cluster-expanded energies of these configurations all lie within 12 meV/CrO<sub>2</sub> of the hull, with many of them less than 1 meV/CrO<sub>2</sub> above the hull. For comparison, the weighted root-mean-square error of our P3 cluster expansion is 6.0 meV/CrO<sub>2</sub> (Section S1, Supporting Information). Thus, there are likely a continuum of (near) ground states in P3 that

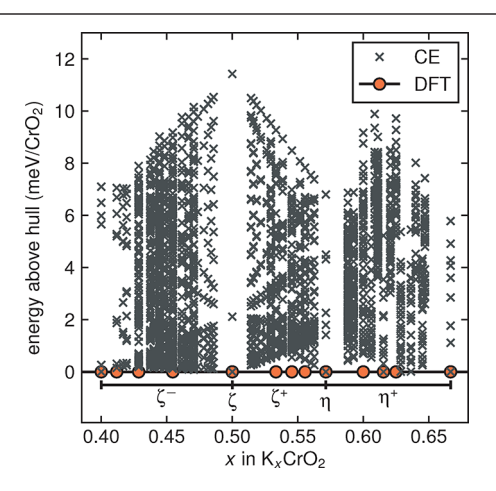


**Figure 4.** Energy above the hull vs composition calculated from the cluster-expanded energies of many hierarchical orderings in P3. The compositions of DFT ground states in P3 are shown at a hull distance of zero. The compositions of important orderings and families of orderings are indicated.

are responsible for the sloping voltage profile seen experimentally.

The other important family of ground state orderings is the M phases, which are stable for  $3/4 \le x \le 7/8$ . First predicted in  $K_x \text{CoO}_{\mathcal{D}}^{54}$  the unique feature of the M phases is a mixture of octahedral and prismatic K coordination within the same layer. The relaxed structures of several representative M orderings are shown in Figure 5. These structures emerge

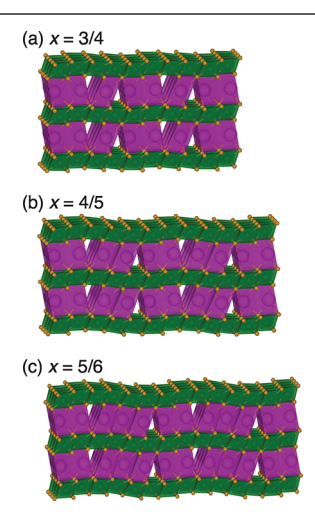


**Figure 5.** Relaxed structures of the ground state M phases at (a) x = 3/4, (b) x = 4/5, and (c) x = 5/6. Structures visualized using VESTA.<sup>29</sup>

when relaxing K-rich orderings in O3 that consist of rows of vacancies (also referred to as O'3 structures). The rows of K on either side of the vacant row relax toward each other to form two adjacent rows of distorted prismatic sites. The displacement of the K causes a periodic undulation of the adjacent CrO<sub>2</sub> layers. The M ground states shown in Figure 5 each contain two rows of prismatic K per unit cell, with varying amounts of octahedral K. The ground states at x = 3/4, x = 4/45, and x = 5/6 contain one, two, and three rows of octahedral K per unit cell, respectively. There are additional low-energy structures belonging to this family that interpolate the simpler structures. For example, the M structure at x = 7/9 (calculated to lie 0.03 meV/CrO<sub>2</sub> above the hull, which is within DFT error) interpolates the ground states at x = 3/4 and x = 4/5, alternating between one and two rows of octahedral K between pairs of prismatic K rows. Therefore, as with the P3 orderings, there is likely an infinite number of M phases with varying numbers of octahedral and prismatic K rows. A complete description of the M phases can be found in ref 54. We also find several metastable M phases below x = 3/4, which are qualitatively different from the row orderings seen above x =3/4 (an example is shown in Figure S4, Supporting Information). Such structures could potentially be accessed during conversion to P3.

**3.3. Structural Evolution.** Our investigation of the phase stability of  $K_xCrO_2$  predicts a complex series of structural transitions upon K extraction that follows the sequence  $O3 \rightarrow M \rightarrow P3 \rightarrow O3$  and passes through a multitude of K-vacancy ordered phases when traversing the M and P3 hosts. Structural transitions often result in abrupt changes in lattice parameters that can have detrimental consequences during cycling of a battery. Figure 6 shows the calculated lattice parameters of configurations on the hulls of each host structure. The

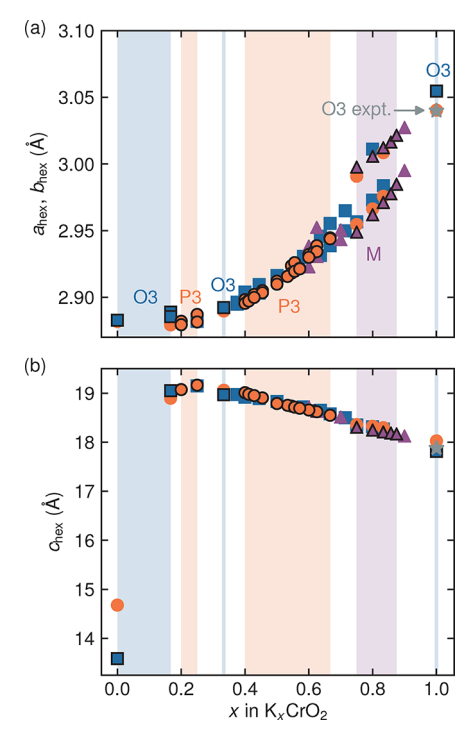


**Figure 6.** Relaxed lattice parameters (in terms of the hexagonal parent structures) vs composition for calculated configurations on the local hull of each host structure. Configurations on the global hull are outlined in black. Colored regions in the background indicate where each host structure is globally stable. Gray stars indicate the experimental lattice parameters of O3-KCrO<sub>2</sub> reported by Kim et al.<sup>23</sup>

lattice parameters of FM O3-KCrO<sub>2</sub> are predicted to be within 0.5% of the experimentally measured values. The removal of K from KCrO<sub>2</sub> leads to a contraction of the in-plane a and b lattice parameters (Figure 6a), which is consistent with the oxidation of  $Cr^{3+}$  toward  $Cr^{4+}$ . A strong splitting of the a and b lattice parameters occurs in the M phases due to the monoclinic distortion that arises from the row ordering among K and vacancies that characterize the M phases. A similar but weaker splitting of the a and b lattice parameters also occurs in the P3 phases. The c lattice parameter increases upon deintercalation until x = 1/3 (Figure 6b), due to the well-known effect of a reduction in screening and an increase in the repulsion between adjacent O layers with the introduction of K vacancies  $\frac{48}{c}$ 

We also simulated X-ray diffraction (XRD) patterns of the relaxed ground state structures to facilitate a direct comparison to the in situ XRD data reported by Kim et al.<sup>23</sup> (Figure 7). Note that slight quantitative differences in peak positions are expected due to discrepancies between the true and calculated lattice parameters. The positions of important peaks observed by Kim et al. are shown as dotted lines and labeled by letters, with an overall shift in composition of  $\Delta x = -0.2$  (determined by adjusting the largest step in the in situ voltage curve until it coincides with x = 1/2, as in Figure 2b). This shift places the starting material at a composition of x = 0.8, which is within the composition interval in which the M phases are predicted to be stable. However, the presence of the hexagonal O3 peaks near 13.7° and 18.0° (labeled a and b in Figure 7), which cannot be clearly attributed to any of our simulated M peaks, implies that the material may start as a metastable two-phase mixture of hexagonal O3 near x = 1 and M near x = 0.8. The three observed peaks labeled c, d, and e in Figure 7 were

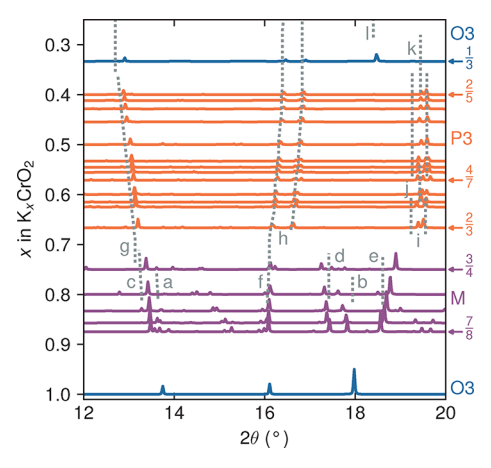


**Figure** 7. Simulated XRD patterns of configurations on the global hull. A wavelength of 0.71073 Å was used, corresponding to Mo  $K\alpha$  radiation. Generated using RIETAN-FP<sup>59</sup> within VESTA.<sup>29</sup> The compositions of certain configurations are indicated with arrows. Gray dotted lines with labels a–l indicate key peaks in the *in situ* XRD patterns from Kim et al. (Figure 4 from ref 23). The composition of the experimental data has been shifted by  $\Delta x = -0.2$ .

attributed to O'3 by Kim et al. but are close to simulated peaks in the M phases. The set of simulated M peaks near 16.0° is also consistent with experimentally observed peaks (labeled f), while the remaining M peaks are significantly less intense and may be difficult to resolve in practice. To test whether the M phases unambiguously provide the best agreement with experiment among the phases considered, we also simulated XRD patterns of the metastable configurations on the local hulls of O3 and P3 in the predicted M stability region (Figure S5, Supporting Information). Neither set of simulated patterns for these metastable structures matches the experimentally observed peaks as closely as that of the M phases, most notably so for the peaks labeled d and e in Figure 7.

At compositions below x = 3/4, the series of observed peaks below 13.5° (labeled g in Figure 7) and near 16.5° (labeled h) match predictions well. The ground state ordering at x = 2/3exhibits a pair of peaks near 19.5° that are consistent with the P'3 peaks reported by Kim et al. (labeled i). Upon reduction of the K composition, these peaks were observed to combine into a single hexagonal P3 peak before splitting again (labeled j); however, ground states predicted in this work show the emergence of a third peak in the same region that then disappears. This occurs near x = 4/7, which is the composition of the  $\eta$  ordering that is predicted to be a ground state. The  $\eta$ ordering has a hexagonal in-plane unit cell (Figure 3d) and may correspond to the experimentally observed hexagonal P3 structure. Below x = 2/5, Kim et al. again observe a single hexagonal P3 peak (labeled k), which could indicate that K begins to disorder in this regime. Finally, a single hexagonal O3 peak was observed near x = 0.3 (labeled 1) close to the O3 peaks of the ground state predicted to be stable at x = 1/3, though this phase may also be disordered. In summary, the simulated XRD patterns largely agree with experimental observations. While the available evidence does not definitively prove the formation of the M phases, it does with some plausibility suggest that their signatures in XRD may have been mistaken for those of O'3 phases.

# 4. DISCUSSION

Our first-principles investigation of phase stability in layered  $K_x CrO_2$  across the full K composition range has revealed the stability of a complex series of phases and K-vacancy orderings. The calculated voltage profile and simulated diffraction patterns are, upon preliminary comparison, consistent with experimental observations, indicating that our description of phase stability in this system is plausible. Our study has produced two key results: A prediction of the stability of hierarchical ground state orderings in P3 that consist of well-ordered domains separated by antiphase boundaries (APBs) and the prediction of the "M" phases, having mixed K coordination, as the stable structures at high K concentrations.

As with many layered transition-metal oxides, K<sub>r</sub>CrO<sub>2</sub> prefers the P3 structure at intermediate K content, as the honeycomb network of trigonal prismatic sites in P3 enables a reduction in K-K repulsion in spite of the fact that those sites share faces with Cr. <sup>28,49</sup> We predict not just several ordered phases, but a continuum of ordered superstructures in P3 that belong to families that share common ordering tendencies (Figure 3). A favorable ordered motif, such as the  $\zeta$  ordering shown in Figure 3a, is preserved over a wide concentration interval, with variations in K concentration accommodated by the introduction of APBs as shown in Figure 3b,c. The P3 orderings are examples of the "Devil's staircase" behavior 60,61 found in many materials, including other layered intercalation compounds<sup>27,53,54,62</sup> and metallic alloys.<sup>63–65</sup> The staircases of P3 orderings discussed here are not unique to K<sub>r</sub>CrO<sub>2</sub>, as they are also the predicted ground states in Na<sub>x</sub>CoO<sub>2</sub> and K,CoO<sub>2</sub>. 53,54 The recurrence of these orderings suggests that they may appear in any P3 system in which electrostatic repulsions between alkali ions are the dominant interactions. It is therefore important to understand the K diffusion behavior within APB-based orderings. Though it is known that strong ordering tends to suppress diffusion, 66,67 the presence of APBs may give rise to unexpected, facile diffusion mechanisms. Future first-principles kinetic studies will explore this possibility. As for the evolution of the APB-based phases during cycling, they could display transitions that occur solely by the rearrangement of boundaries rather than by a nucleation and growth process.

The more surprising prediction of this study is the stability of the M phases—ground states with a mixture of octahedral and prismatic K in the same layer (Figure 5). These structures were first identified computationally in  $K_xCoO_2$ , <sup>54</sup> emerging from spontaneous relaxations of certain O3 structures. The unique stability of these undulating phases appears to originate from an in-layer rearrangement of K that allows them to spread out more than is possible in O3. The resulting reduction in K–K repulsion outweighs the strain penalty of warping the metal oxide layers. <sup>54</sup> In  $K_xCoO_2$  the M phases are predicted to appear above the K compositions investigated electrochemically <sup>11</sup> and are likely not globally stable. As layered  $K_xCrO_2$  is stable up to x = 1, <sup>23</sup> it is more likely to exhibit the M phases.

Our simulated XRD results (Figure 7) suggest that the M phases have diffraction patterns that are very similar to those assigned to monoclinic O'3 structures, to the point where it may be challenging to differentiate between the two. The energies of the M phases are significantly lower than the closest O3 or P3 configurations considered in this study, and the difference increases with x (Figure S2, Supporting Information). For example, at x = 3/4 the M ground state lies 17 meV/

CrO<sub>2</sub> below the O3 ground state and 5 meV/CrO<sub>2</sub> below the P3 ground state, while at x = 5/6 M lies 33 meV/CrO<sub>2</sub> below O3 and 35 meV/CrO<sub>2</sub> below P3. The sizable energetic preference for the M phases does not support the idea that O3 or P3 would form in their place. We have also confirmed that M phases provide a better match to the experimentally observed XRD data than the metastable O3 or P3 structures (Figure S5, Supporting Information). We note that the formation of an M phase within an O3 or P3 electrode particle during cycling would result in coherency strain due to lattice mismatch and the warping of the CrO2 layers. Such strain could potentially be quantified in XRD studies through analysis of peak broadening. 68,69 We also observe that the calculated lattice parameters of the M phases lie between those of the end point O3-KCrO2 and P3-K2/3CrO2 phases and are comparable to those of the most stable O3 and P3 structures in the M stability region (Figure S5, Supporting Information). This observation, along with the presence of metastable M phases below x = 3/4 (Figure S4, Supporting Information), suggests that the M phases could offer a continuous pathway for structural transformation from O3 to P3 as K is extracted.

If the M phases do indeed form, there would be important consequences for battery performance. The strain associated with forming the M phases upon charge could result in a significant overpotential, which may be part of the reason that the calculated voltage curve underpredicts experiment at high x (Figure 2b). The M phases may also explain the capacity loss observed experimentally, where K cannot be fully reinserted into the cathode at the end of first discharge. Kim et al. attributed this to slow kinetics in the O'3 phase, 23 but it could be that the strongly ordered M phases suppress the transition back to the O3 phase altogether. It therefore may be favorable to make chemical substitutions that penalize the formation of the M phases or facilitate reversible transitions between M and O3, if possible. Layered cathode materials engineered to avoid such detrimental phase transitions while remaining stable at high K concentrations could allow for the low-voltage regime to be fully utilized.

# 5. CONCLUSION

This study investigated phase stability in layered K<sub>x</sub>CrO<sub>2</sub>, a promising cathode material for K-ion batteries. We found that O3 tends to be stable at extreme K concentrations, while P3 is stable at intermediate ones. A multitude of (near) ground state structures appear in P3, belonging to several families of hierarchical in-layer K orderings based on the stable x = 1/2and x = 4/7 orderings. Antiphase boundaries between the ordered domains allow for smooth variations in composition with K (de)intercalation but may limit the speed and dimensionality of diffusion. We also predict the emergence of unusual "M" phases at high x (3/4  $\leq x \leq$  7/8) that contain mixed octahedral and prismatic K coordination within each intercalation layer. These phases display large distortions driven by K-K repulsion and may lead to irreversiblities if they form during cycling. We find that the formation of the M phases is plausible and that they may be difficult to distinguish from O'3 phases. Our calculated voltage profile and simulated XRD patterns are generally consistent with experimental observations, assuming a K-deficient starting material. These results should provide a foundation for understanding and optimizing layered oxide cathodes with near-maximal K content to unlock higher capacities in battery applications.

## ASSOCIATED CONTENT

# Supporting Information

The Supporting Information is available free of charge at https://pubs.acs.org/doi/10.1021/acs.chemmater.0c01460.

Details of cluster expansions and Monte Carlo simulations, link to repository of density functional theory calculation results (including relaxed structures), global hull distances, energies of nonferromagnetic orderings, example of a metastable M ordering, and simulated X-ray diffraction patterns of metastable O3 and P3 phases (PDF)

# AUTHOR INFORMATION

# **Corresponding Author**

Anton Van der Ven – Materials Department, University of California, Santa Barbara, Santa Barbara, California 93106, United States; Email: avdv@ucsb.edu

#### **Author**

Jonas L. Kaufman — Materials Department, University of California, Santa Barbara, Santa Barbara, California 93106, United States; Occid.org/0000-0002-0814-9462

Complete contact information is available at: https://pubs.acs.org/10.1021/acs.chemmater.0c01460

#### Notes

The authors declare no competing financial interest.

#### ACKNOWLEDGMENTS

J.L.K. thanks Julija Vinckevičiūtė for many helpful discussions. J.L.K. acknowledges support from the United States Department of Energy through the Computational Science Graduate Fellowship (DOE CSGF) under Grant Number DE-FG02-97ER25308. This work was supported as part of the Center for Synthetic Control Across Length-scales for Advancing Rechargeables (SCALAR), an Energy Frontier Research Center funded by the U.S. Department of Energy, Office of Science, Basic Energy Sciences under Award No. DE-SC0019381. Use was made of computational facilities purchased with funds from the National Science Foundation (CNS-1725797) and administered by the Center for Scientific Computing (CSC). The CSC is supported by the California NanoSystems Institute and the Materials Research Science and Engineering Center (MRSEC; NSF DMR 1720256) at UC Santa Barbara. This research used resources of the National Energy Research Scientific Computing Center (NERSC), a U.S. Department of Energy Office of Science User Facility operated under Contract No. DE-AC02-05CH11231.

## REFERENCES

- (1) Dennis, K.; Colburn, K.; Lazar, J. Environmentally beneficial electrification: The dawn of 'emissions efficiency'. *Electricity Journal* **2016**, 29, 52–58.
- (2) Olivetti, E. A.; Ceder, G.; Gaustad, G. G.; Fu, X. Lithium-Ion Battery Supply Chain Considerations: Analysis of Potential Bottlenecks in Critical Metals. *Joule* **2017**, *1*, 229–243.
- (3) Kubota, K.; Dahbi, M.; Hosaka, T.; Kumakura, S.; Komaba, S. Towards K-Ion and Na-Ion Batteries as "Beyond Li-Ion. *Chem. Rec.* **2018**, *18*, 459–479.
- (4) Delmas, C. Sodium and Sodium-Ion Batteries: 50 Years of Research. Adv. Energy Mater. 2018, 8, 1703137.

- (5) Hosaka, T.; Kubota, K.; Hameed, A. S.; Komaba, S. Research Development on K-Ion Batteries. *Chem. Rev.* **2020**, *XXXX*, *XXX*—*XXX*.
- (6) Komaba, S.; Hasegawa, T.; Dahbi, M.; Kubota, K. Potassium intercalation into graphite to realize high-voltage/high-power potassium-ion batteries and potassium-ion capacitors. *Electrochem. Commun.* **2015**, *60*, 172–175.
- (7) Sha, M.; Liu, L.; Zhao, H.; Lei, Y. Review on Recent Advances of Cathode Materials for Potassium-ion Batteries. *Energy Environ. Mater.* **2020**, *3*, 56–66.
- (8) Rajagopalan, R.; Tang, Y.; Ji, X.; Jia, C.; Wang, H. Advancements and Challenges in Potassium Ion Batteries: A Comprehensive Review. *Adv. Funct. Mater.* **2020**, *30*, 1909486.
- (9) Han, M. H.; Gonzalo, E.; Singh, G.; Rojo, T. A comprehensive review of sodium layered oxides: powerful cathodes for Na-ion batteries. *Energy Environ. Sci.* **2015**, *8*, 81–102.
- (10) Vaalma, C.; Giffin, G. A.; Buchholz, D.; Passerini, S. Non-Aqueous K-Ion Battery Based on Layered K0.3MnO2 and Hard Carbon/Carbon Black. *J. Electrochem. Soc.* **2016**, *163*, A1295.
- (11) Hironaka, Y.; Kubota, K.; Komaba, S. P2- and P3-K x CoO 2 as an electrochemical potassium intercalation host. *Chem. Commun.* **2017**, 53, 3693–3696.
- (12) Kim, H.; Kim, J. C.; Bo, S.-H.; Shi, T.; Kwon, D.-H.; Ceder, G. K-Ion Batteries Based on a P2-Type K0.6CoO2 Cathode. *Adv. Energy Mater.* **2017**, *7*, 1700098.
- (13) Kim, H.; Seo, D.-H.; Kim, J. C.; Bo, S.-H.; Liu, L.; Shi, T.; Ceder, G. Investigation of Potassium Storage in Layered P3-Type K0.5MnO2 Cathode. *Adv. Mater.* **2017**, *29*, 1702480.
- (14) Liu, C.; Luo, S.; Huang, H.; Wang, Z.; Hao, A.; Zhai, Y.; Wang, Z. K0.67Ni0.17Co0.17Mn0.66O2: A cathode material for potassiumion battery. *Electrochem. Commun.* **2017**, *82*, 150–154.
- (15) Wang, X.; Xu, X.; Niu, C.; Meng, J.; Huang, M.; Liu, X.; Liu, Z.; Mai, L. Earth Abundant Fe/Mn-Based Layered Oxide Interconnected Nanowires for Advanced K-Ion Full Batteries. *Nano Lett.* **2017**, *17*, 544–550.
- (16) Nathan, M. G. T.; Naveen, N.; Park, W. B.; Sohn, K.-S.; Pyo, M. Fast chargeable P2–K2/3[Ni1/3Mn2/3]O2 for potassium ion battery cathodes. *J. Power Sources* **2019**, 438, 226992.
- (17) Zhang, H.; Xi, K.; Jiang, K.; Zhang, X.; Liu, Z.; Guo, S.; Zhou, H. Enhanced K-ion kinetics in a layered cathode for potassium ion batteries. *Chem. Commun.* **2019**, *55*, 7910–7913.
- (18) Zhang, Q.; Didier, C.; Pang, W. K.; Liu, Y.; Wang, Z.; Li, S.; Peterson, V. K.; Mao, J.; Guo, Z. Structural Insight into Layer Gliding and Lattice Distortion in Layered Manganese Oxide Electrodes for Potassium-Ion Batteries. *Adv. Energy Mater.* **2019**, *9*, 1900568.
- (19) Gao, A.; Li, M.; Guo, N.; Qiu, D.; Li, Y.; Wang, S.; Lu, X.; Wang, F.; Yang, R. K-Birnessite Electrode Obtained by Ion Exchange for Potassium-Ion Batteries: Insight into the Concerted Ionic Diffusion and K Storage Mechanism. *Adv. Energy Mater.* **2019**, *9*, 1802739.
- (20) Choi, J. U.; Ji Park, Y.; Jo, J. H.; Jung, Y. H.; Ahn, D.-C.; Jeon, T.-Y.; Lee, K.-S.; Kim, H.; Lee, S.; Kim, J.; Myung, S.-T. An optimized approach toward high energy density cathode material for K-ion batteries. *Energy Storage Materials* **2020**, 27, 342–351.
- (21) Delmas, C.; Devalette, M.; Fouassier, C.; Hagenmuller, P. Les phases KXCrO2 ( $X \le 1$ ). *Mater. Res. Bull.* 1975, 10, 393–398.
- (22) Fouassier, C.; Delmas, C.; Hagenmuller, P. Evolution structurale et proprietes physiques des phases AXMO2 (A = Na, K; M = Cr, Mn, Co) ( $x \le 1$ ). *Mater. Res. Bull.* 1975, 10, 443–449.
- (23) Kim, H.; Seo, D.-H.; Urban, A.; Lee, J.; Kwon, D.-H.; Bo, S.-H.; Shi, T.; Papp, J. K.; McCloskey, B. D.; Ceder, G. Stoichiometric Layered Potassium Transition Metal Oxide for Rechargeable Potassium Batteries. *Chem. Mater.* **2018**, *30*, 6532–6539.
- (24) Hwang, J.-Y.; Kim, J.; Yu, T.-Y.; Myung, S.-T.; Sun, Y.-K. Development of P3-K0.69CrO2 as an ultra-high-performance cathode material for K-ion batteries. *Energy Environ. Sci.* **2018**, *11*, 2821–2827.
- (25) Naveen, N.; Han, S. C.; Singh, S. P.; Ahn, D.; Sohn, K.-S.; Pyo, M. Highly stable P'3-K0.8CrO2 cathode with limited dimensional

- changes for potassium ion batteries. *J. Power Sources* **2019**, 430, 137–144
- (26) Delmas, C.; Braconnier, J.-J.; Fouassier, C.; Hagenmuller, P. Electrochemical intercalation of sodium in NaxCoO2 bronzes. *Solid State Ionics* **1981**, 3–4, 165–169.
- (27) Vinckevičiūtė, J.; Radin, M. D.; Van der Ven, A. Stacking-Sequence Changes and Na Ordering in Layered Intercalation Materials. *Chem. Mater.* **2016**, 28, 8640–8650.
- (28) Kaufman, J. L.; Vinckevičiūtė, J.; Krishna Kolli, S.; Gabriel Goiri, J.; Van der Ven, A. Understanding intercalation compounds for sodium-ion batteries and beyond. *Philos. Trans. R. Soc., A* **2019**, 377, 20190020.
- (29) Momma, K.; Izumi, F. VESTA 3 for three-dimensional visualization of crystal, volumetric and morphology data. *J. Appl. Crystallogr.* **2011**, *44*, 1272–1276.
- (30) Kresse, G.; Hafner, J. Ab initio molecular dynamics for liquid metals. *Phys. Rev. B: Condens. Matter Mater. Phys.* **1993**, 47, 558–561.
- (31) Kresse, G.; Hafner, J. Ab initio molecular-dynamics simulation of the liquid-metal—amorphous-semiconductor transition in germanium. *Phys. Rev. B: Condens. Matter Mater. Phys.* **1994**, 49, 14251—14269.
- (32) Kresse, G.; Furthmüller, J. Efficiency of ab-initio total energy calculations for metals and semiconductors using a plane-wave basis set. *Comput. Mater. Sci.* **1996**, *6*, 15–50.
- (33) Kresse, G.; Furthmüller, J. Efficient iterative schemes for ab initio total-energy calculations using a plane-wave basis set. *Phys. Rev. B: Condens. Matter Mater. Phys.* **1996**, *54*, 11169–11186.
- (34) Blöchl, P. E. Projector augmented-wave method. *Phys. Rev. B: Condens. Matter Mater. Phys.* **1994**, *50*, 17953–17979.
- (35) Kresse, G.; Joubert, D. From ultrasoft pseudopotentials to the projector augmented-wave method. *Phys. Rev. B: Condens. Matter Mater. Phys.* **1999**, *59*, 1758–1775.
- (36) Monkhorst, H. J.; Pack, J. D. Special points for Brillouin-zone integrations. *Phys. Rev. B* **1976**, *13*, 5188–5192.
- (37) Sun, J.; Ruzsinszky, A.; Perdew, J. P. Strongly Constrained and Appropriately Normed Semilocal Density Functional. *Phys. Rev. Lett.* **2015**, *115*, 036402.
- (38) Sun, J.; Remsing, R. C.; Zhang, Y.; Sun, Z.; Ruzsinszky, A.; Peng, H.; Yang, Z.; Paul, A.; Waghmare, U.; Wu, X.; Klein, M. L.; Perdew, J. P. Accurate first-principles structures and energies of diversely bonded systems from an efficient density functional. *Nat. Chem.* **2016**, *8*, 831–836.
- (39) Chakraborty, A.; Dixit, M.; Aurbach, D.; Major, D. T. Predicting accurate cathode properties of layered oxide materials using the SCAN meta-GGA density functional. *npj Comput. Mater.* **2018**, *4*, 60.
- (40) Kitchaev, D. A.; Peng, H.; Liu, Y.; Sun, J.; Perdew, J. P.; Ceder, G. Energetics of MnO<sub>2</sub> polymorphs in density functional theory. *Phys. Rev. B: Condens. Matter Mater. Phys.* **2016**, 93, 045132.
- (41) Yang, J. H.; Kitchaev, D. A.; Ceder, G. Rationalizing accurate structure prediction in the meta-GGA SCAN functional. *Phys. Rev. B: Condens. Matter Mater. Phys.* **2019**, *100*, 035132.
- (42) Blöchl, P. E.; Jepsen, O.; Andersen, O. K. Improved tetrahedron method for Brillouin-zone integrations. *Phys. Rev. B: Condens. Matter Mater. Phys.* **1994**, 49, 16223–16233.
- (43) CASM Developers. CASM v0.2.X, 2020. Available from https://github.com/prisms-center/CASMcode.
- (44) Thomas, J. C.; Van der Ven, A. Finite-temperature properties of strongly anharmonic and mechanically unstable crystal phases from first principles. *Phys. Rev. B: Condens. Matter Mater. Phys.* **2013**, 88, 214111.
- (45) Van der Ven, A.; Thomas, J.; Puchala, B.; Natarajan, A. First-Principles Statistical Mechanics of Multicomponent Crystals. *Annu. Rev. Mater. Res.* **2018**, 48, 27–55.
- (46) Puchala, B.; Van der Ven, A. Thermodynamics of the Zr-O system from first-principles calculations. *Phys. Rev. B: Condens. Matter Mater. Phys.* **2013**, *88*, 094108.

- (47) Van der Ven, A.; Deng, Z.; Banerjee, S.; Ong, S. P. Rechargeable Alkali-Ion Battery Materials: Theory and Computation. *Chem. Rev.* **2020**, DOI: 10.1021/acs.chemrev.9b00601.
- (48) Van der Ven, A.; Aydinol, M. K.; Ceder, G.; Kresse, G.; Hafner, J. First-principles investigation of phase stability in Li<sub>x</sub>CoO<sub>2</sub>. *Phys. Rev. B: Condens. Matter Mater. Phys.* **1998**, *58*, 2975–2987.
- (49) Radin, M. D.; Van der Ven, A. Stability of Prismatic and Octahedral Coordination in Layered Oxides and Sulfides Intercalated with Alkali and Alkaline-Earth Metals. *Chem. Mater.* **2016**, 28, 7898–7904
- (50) Delmas, C.; Le Flem, G.; Fouassier, C.; Hagenmuller, P. Etude comparative des proprietes magnetiques des oxydes lamellaires ACrO2 (A = Li, Na, K)—II: Calcul des integrales d'echange. *J. Phys. Chem. Solids* **1978**, *39*, 55–57.
- (51) Soubeyroux, J. L.; Fruchart, D.; Delmas, C.; Le Flem, G. Neutron powder diffraction studies of two-dimensional magnetic oxides. *J. Magn. Magn. Mater.* 1979, 14, 159–162.
- (52) Radin, M. D.; Hy, S.; Sina, M.; Fang, C.; Liu, H.; Vinckeviciute, J.; Zhang, M.; Whittingham, M. S.; Meng, Y. S.; der Ven, A. V. Narrowing the Gap between Theoretical and Practical Capacities in Li-Ion Layered Oxide Cathode Materials. *Adv. Energy Mater.* **2017**, *7*, 1602888.
- (53) Kaufman, J. L.; Van der Ven, A. Na<sub>x</sub>CoO<sub>2</sub> phase stability and hierarchical orderings in the O3/P3 structure family. *Phys. Rev. Mater.* **2019**, *3*, 015402.
- (54) Toriyama, M. Y.; Kaufman, J. L.; Van der Ven, A. Potassium ordering and structural phase stability in layered K<sub>x</sub>CoO<sub>2</sub>. *ACS Appl. Energy Mater.* **2019**, *2*, 2629–2636.
- (55) Kubota, K.; Asari, T.; Yoshida, H.; Yaabuuchi, N.; Shiiba, H.; Nakayama, M.; Komaba, S. Understanding the Structural Evolution and Redox Mechanism of a NaFeO2–NaCoO2 Solid Solution for Sodium-Ion Batteries. *Adv. Funct. Mater.* **2016**, *26*, 6047–6059.
- (56) Yabuuchi, N.; Ikeuchi, I.; Kubota, K.; Komaba, S. Thermal Stability of NaxCrO2 for Rechargeable Sodium Batteries; Studies by High-Temperature Synchrotron X-ray Diffraction. *ACS Appl. Mater. Interfaces* **2016**, *8*, 32292–32299.
- (57) Woodford, W. H.; Carter, W. C.; Chiang, Y.-M. Design criteria for electrochemical shock resistant battery electrodes. *Energy Environ. Sci.* **2012**, *5*, 8014–8024.
- (58) Liu, H.; Wolf, M.; Karki, K.; Yu, Y.-S.; Stach, E. A.; Cabana, J.; Chapman, K. W.; Chupas, P. J. Intergranular Cracking as a Major Cause of Long-Term Capacity Fading of Layered Cathodes. *Nano Lett.* **2017**, *17*, 3452–3457.
- (59) Izumi, F.; Momma, K. Three-dimensional visualization in powder diffraction. *Solid State Phenom.* **2007**, *130*, 15–20.
- (60) Bak, P.; von Boehm, J. Ising model with solitons, phasons, and "the devil's staircase. *Phys. Rev. B: Condens. Matter Mater. Phys.* **1980**, 21, 5297–5308.
- (61) Kanamori, J. Infinite Series of Ground States of the Ising Model on the Honeycomb Lattice. J. Phys. Soc. Jpn. 1984, 53, 250–260.
- (62) Vitoux, L.; Guignard, M.; Suchomel, M. R.; Pramudita, J. C.; Sharma, N.; Delmas, C. The NaxMoO2 Phase Diagram ( $1/2 \le x < 1$ ): An Electrochemical Devil's Staircase. *Chem. Mater.* **2017**, 29, 7243–7254.
- (63) Decolvenaere, E.; Gordon, M. J.; Van der Ven, A. Testing predictions from density functional theory at finite temperatures:  $\beta_2$ -like ground states in Co-Pt. *Phys. Rev. B: Condens. Matter Mater. Phys.* **2015**, 92, 085119.
- (64) Natarajan, A. R.; Solomon, E. L. S.; Puchala, B.; Marquis, E. A.; Van der Ven, A. On the early stages of precipitation in dilute Mg–Nd alloys. *Acta Mater.* **2016**, *108*, 367–379.
- (65) Goiri, J. G.; Van der Ven, A. Phase and structural stability in Ni-Al systems from first principles. *Phys. Rev. B: Condens. Matter Mater. Phys.* **2016**, *94*, 094111.
- (66) Shu, G. J.; Chou, F. C. Sodium-ion diffusion and ordering in single-crystal P2-Na<sub>x</sub>CoO<sub>2</sub>. *Phys. Rev. B: Condens. Matter Mater. Phys.* **2008**, 78, 052101.
- (67) Willis, T. J.; Porter, D. G.; Voneshen, D. J.; Uthayakumar, S.; Demmel, F.; Gutmann, M. J.; Roger, M.; Refson, K.; Goff, J. P.

Diffusion mechanism in the sodium-ion battery material sodium cobaltate. Sci. Rep. 2018, 8, 3210.

- (68) Williamson, G. K.; Hall, W. H. X-ray line broadening from filed aluminium and wolfram. *Acta Metall.* **1953**, *1*, 22–31.
- (69) Fell, C. R.; Chi, M.; Meng, Y. S.; Jones, J. L. In situ X-ray diffraction study of the lithium excess layered oxide compound Li[Li0.2Ni0.2Mn0.6]O2 during electrochemical cycling. *Solid State Ionics* **2012**, 207, 44–49.

Article